J. Fluid Mech. (2021), *vol*. 919, A40, doi:10.1017/jfm.2021.421

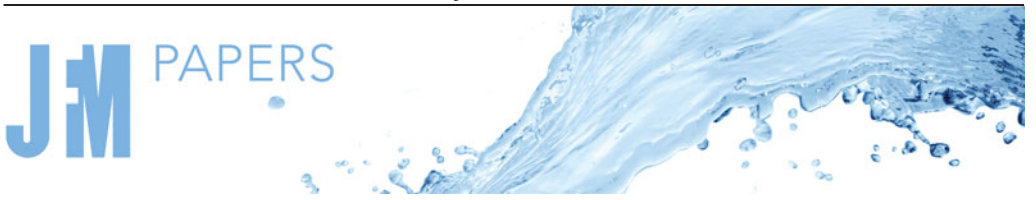

A study on the RR-to-MR transition of shock wave reflections near the leading edge in hypersonic flows

Longsheng Xue[1,2], **Chengpeng Wang**[1,2,†] **and Keming Cheng**[1,2]

[1]College of Aerospace Engineering, Nanjing University of Aeronautics and Astronautics, Yudao Street 29, Nanjing, Jiangsu 210016, PR China

[2]Key Laboratory of Unsteady Aerodynamics and Flow Control, Ministry of Industry and Information Technology, Nanjing University of Aeronautics and Astronautics, Yudao Street 29, Nanjing, Jiangsu 210016, PR China

(Received 30 December 2020; revised 11 March 2021; accepted 8 May 2021)

In this paper, the incident shock–separation shock interactions on a surface plate near the leading edge are studied theoretically and experimentally, and the transition from regular reflection (RR) to Mach reflection (MR) is the main focus. The theoretical method employs free interaction theory (FIT) and the minimum entropy production (MEP) principle to analyse the separation shock strength of flow separated from the boundary layer and separated from the leading edge, respectively, the criterion based on the MEP principle is employed to predict the RR-to-MR transition near the leading edge. The experiments were performed on a rotatable wedge situated over a sharp leading-edge plate such that the wedge could continuously change the flow deflection angle from 0° to 40° by means of a high-precision control device. Fast-response transducers and a high-speed camera were used to measure dynamic pressures and to take schlieren images, respectively. The influences of wedge positions, Reynolds numbers and Mach numbers on shock reflections are investigated by careful tests. The theoretical and experimental results for Mach numbers 5, 6, 7 and 8 show good agreement, indicating that the theoretical method is applicable.

Key words: flow–structure interactions, high-speed flow, boundary-layer separation

1. Introduction

Shock wave reflections as well as configuration transitions are classical topics and fundamental phenomena in supersonic flow. The reflection configurations are normally characterised by shock–shock interactions, shock–boundary layer interactions and

† Email address for correspondence: wangcp@nuaa.edu.cn

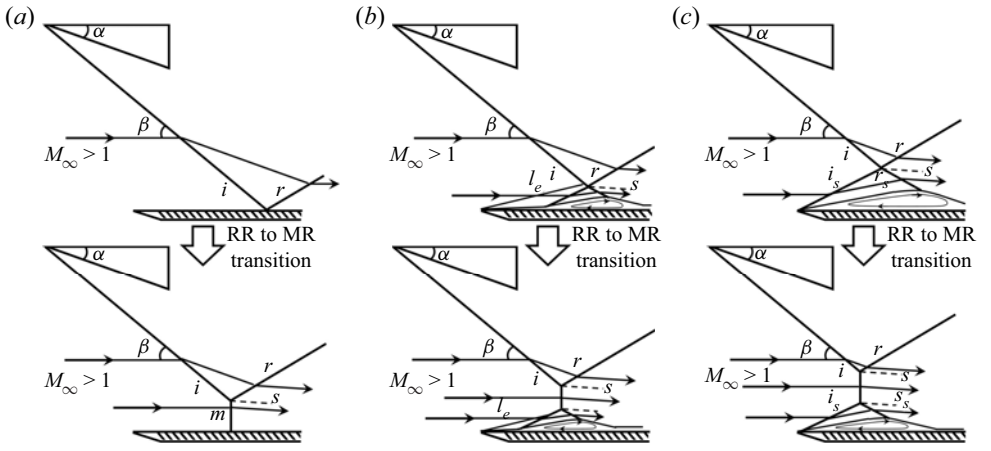

Figure 1. Schematic illustration of the RR-to-MR transition on a plate: (*a*) perfect inviscid flow, (*b*) flow separated from the boundary layer and (*c*) flow separated from the leading edge.

shock–separation region interactions, which exist widely in the flow fields of supersonic vehicle bodies, inlets and nozzles.

For a perfect inviscid flow, shock reflection on a plate includes regular reflection (RR) and irregular reflection. The former consists of an incident shock i and a reflected shock r, the latter is commonly characterised by Mach reflection (MR), which consists of an incident shock i, a reflected shock r, slip line s and Mach stem m, as shown in figure 1(*a*). Early classical theory (see von Neumann 1943, 1945) attributes reflection configurations to incoming Mach number M_∞ and flow deflection angle α and the configuration is determined by two criteria: one is named the von Neumann criterion α_{vn}, and the other is the detachment criterion α_D. RR exists in flows of $\alpha < \alpha_{vn}$, MR exists in flows of $\alpha > \alpha_D$, and both RR and MR could exist in flows of $\alpha_{vn} \leq \alpha \leq \alpha_D$. However, owing to the viscous effect, the flow pattern near the leading edge with the simple shock wave–wall interaction shown in figure 1(*a*) does not exist, and the much more complex configurations shown in figures 1(*b*) and 1(*c*) are more common, indicating that the classical inviscid criteria might not predict the RR-to-MR transition well.

Taking separation shock into consideration, the MR is similar to the asymmetric shock–shock interaction, in which a relatively strong incident shock i and a separation shock i_s are connected by a Mach stem m, generating two reflected shock waves r and r_s, as well as two slip lines s and s_s. Owing to the separation shock, the RR-to-MR transition cannot be predicted by inviscid theory, which can be explained with shock polar lines. As shown in figure 2(*a*), the incident shock polar line is divided by α_{vn} and α_D into three solution domains: the RR domain, dual-solution domain and MR domain. The reflected shock polar lines demonstrate that although the given flow deflection angle α is larger than the detachment criterion α_D, which resides in the MR domain, the unknown flow deflection angle α_s of the separation region changes the criteria and results in various possible configurations, including RR and MR, as shown in figures 2(*b*), 2(*c*) and 2(*d*). The RR-to-MR transition related to separation shock has been observed in several recent studies (see Matheis & Hickel 2015; Grossman & Bruce 2018). Therefore, the RR-to-MR transition near the leading edge is determined not only by the incident shock strength but also by the separation shock strength, which could be affected by the leading-edge shock, boundary layer and the separation shock.

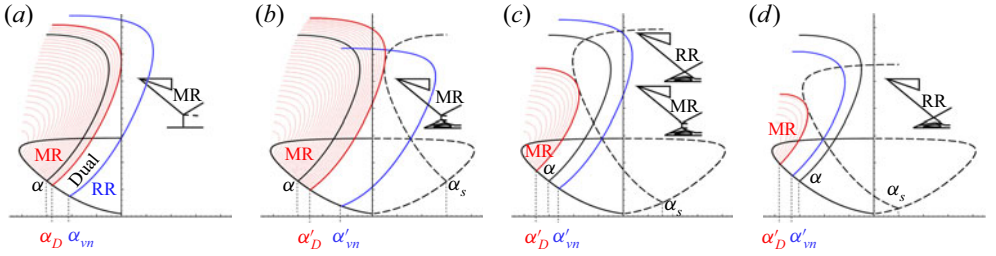

Figure 2. Shock polar lines of possible solutions based on a given flow deflection angle: (*a*) MR solution of an inviscid flow, (*b*) MR solution considering separation shock, (*c*) dual solution considering separation shock and (*d*) RR solution for separation shock.

Separation of a boundary layer might differ from separation at a sharp leading edge. For the flow pattern in figure 1(*b*), assume that the leading-edge shock is very weak, the shock reflection could be treated as free interaction, which is related to the boundary layer. If the boundary layer is considered the dominant influencing factor on the reflection configuration, then free interaction theory (FIT) could be employed to estimate the separation shock strength (see Chapman, Kuehn & Larson 1958). Shock reflection thickens the boundary layer and results in a pressure rise. FIT establishes the relation between the pressure rise and boundary flow properties by the following equation:

$$\frac{p_s}{p_\infty} = 1 + F(\bar{x})\gamma {M_\infty}^2 \sqrt{\frac{C_{f0}}{2({M_\infty}^2 - 1)^{0.5}}}, \tag{1.1}$$

where p_s represents the static pressure in the separation region, γ is the specific heat ratio, C_{f0} is the skin-friction coefficient, which could be estimated according to incoming flow conditions (see Tao, Fan & Zhao 2014) and $F(\bar{x})$ is a universal correlation function, which is independent of Mach and Reynolds numbers. Erdos & Pallone (1962) proposed specific values $F(\bar{x})_{lam0} \approx 0.81$ at the separation point and $F(\bar{x})_{lam1} \approx 1.47$ for the plateau pressure in laminar flows and $F(\bar{x})_{tur0} \approx 4.22$ and $F(\bar{x})_{tur1} \approx 6.00$ for turbulent flows. The separation shock strength for a given Mach number M_∞ and skin-friction coefficient C_{f0} is therefore determined.

FIT states that the scaling of the first part of the interaction should only depend upon upstream flow properties and not on the downstream flow conditions, e.g. shock wave reflections or geometrical confinement. The validation of FIT can be widely found in the literature (see Hakkinen *et al.* 1959; Babinsky & Harvey 2011; Matheis & Hickel 2015; Giepman *et al.* 2018). However, the universal correlation function $F(\bar{x})$, for the pressure plateau could be affected by various influences, resulting in various values being found in the literature. Zheltovodov & Yakovlev (1986) and Zheltovodov (1996) reported a plateau value of $F(\bar{x})_{tur1} \approx 7.4$. Tao *et al.* (2014) employed $F(\bar{x})_{tur1} \approx 8.5$ according to the experimental conditions. Matheis & Hickel (2015) proposed $F(\bar{x})_{tur1} \approx 6.3$ based on the results of large-eddy simulations. In the study on relatively weak interactions in laminar flow conducted by Giepman *et al.* (2018), it was observed that the incipient separation threshold was presented as a band rather than a sharp line, and that the incident shock angles (or flow deflection angles) and Mach numbers could distinctly affect the peak value of $F(\bar{x})$, as shown in figure 3(*a*,*b*), where the theoretical pressure plateau was not reached. In addition, the experiments in turbulent flow conducted by Grossman & Bruce (2018) prove that geometrical confinements could also obviously affect the interactions, as shown

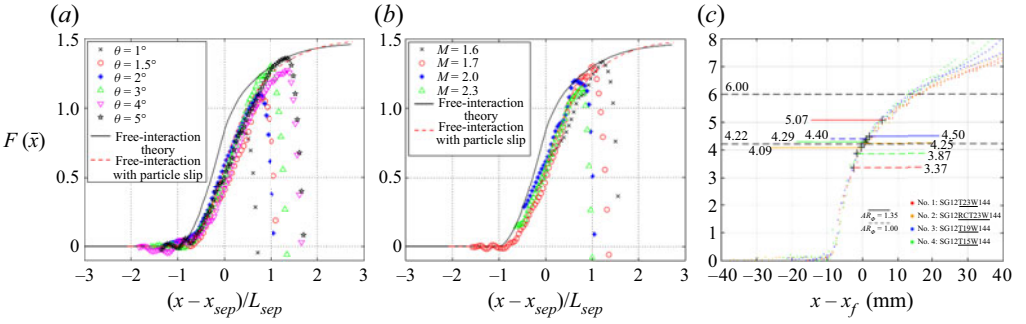

Figure 3. Correlation function $F(\bar{x})$ in the literature: (*a*) laminar interactions on various flow deflection angles (see Giepman, Schrijer & van Oudheusden 2018), (*b*) laminar interactions on various free-stream Mach numbers (see Giepman *et al.* 2018) and (*c*) turbulent interactions on various geometrical confinements (see Grossman & Bruce 2018).

in figure 3(*c*). Thus, FIT might only be applicable up to the point of separation and responsible for some initial contributions to the separation shock.

Several recent studies (see Matheis & Hickel 2015; Giepman *et al.* 2018; Xue *et al.* 2020) found that the size of the separation bubble is strongly related to the incident shock strength. In the study of Xue *et al.* (2020), it was observed that the separation shock strength close to the interaction point was positively correlated with incident shock, and the separation shock strength in MR was stronger than that in RR, causing difficulty in predicting the RR-to-MR transition. Even though the shock reflection region is so close to the plate leading edge that the boundary layer almost disappears, a separation bubble still exists (see Sriram *et al.* 2016). For the flow pattern in figure 1(*c*), if a separation bubble is considered the dominant influencing factor on shock reflections, then the flow configuration can be treated as an incident shock–separation shock interaction, and then, the minimum entropy production (MEP) principle can be employed to analyse asymmetric shock–shock reflections. Li & Ben-Dor (1996*a*,*b*) first attempted to employ the MEP principle to analyse shock–shock interactions in steady flow and unsteady flow, and the results agreed well with experiments conducted by Chpoun *et al.* (1995). Accordingly, Wang, Xue & Cheng (2018) employed the MEP principle to analyse separation shock–separation shock interactions induced by downstream back pressure, and the results agreed well with experimental results. Notably, in both the works of Li & Ben-Dor (1996*a*,*b*) and Wang *et al.* (2018), the influence of the boundary layer did not have to be taken into consideration. However, in the study of Xue *et al.* (2020) on shock wave–boundary layer interactions, the boundary layer could not be neglected. Thus, both FIT and the MEP principle were employed, resulting in curved separation shocks owing to various combinations of FIT solutions and MEP solutions, while the RR-to-MR transition was not predicted well.

In summary, the inviscid criteria cannot predict the RR-to-MR transition near the leading edge, and the shock strength in viscous separation flow should therefore be determined first. In the current work, the incident shock–separation shock interaction is the focus, and a criterion based on the MEP principle is employed to predict the RR-to-MR transition near the leading edge. Aiming to solve these problems, the theoretical methods are discussed in detail, and for verification, experiments are performed at various Mach numbers, including 5, 6, 7 and 8, on a test model of a shock generator, which can change the wedge angle continuously from 0° to 40° through a high-precision control device.

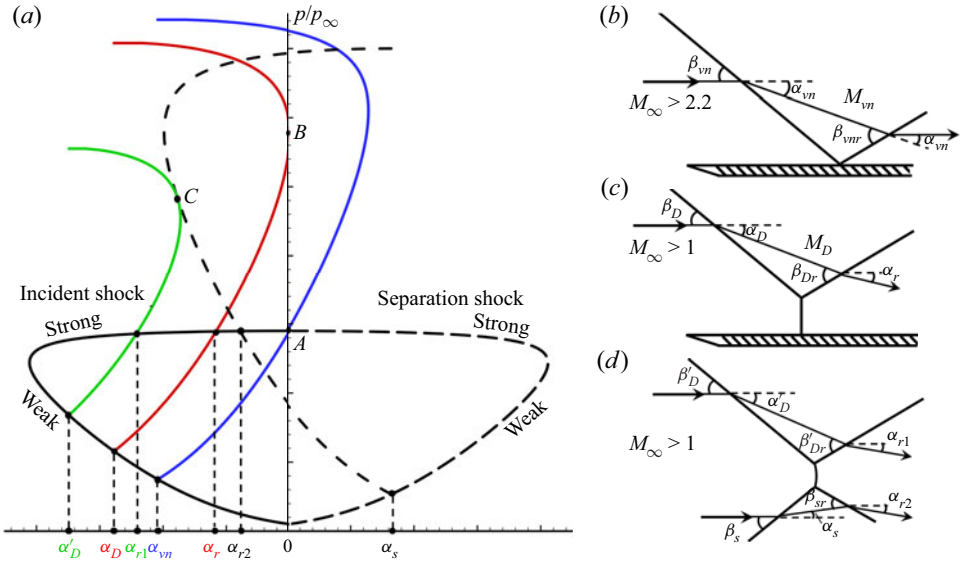

Figure 4. Illustration of the shock reflection criteria: (*a*) shock polar lines, (*b*) inviscid RR, (*c*) inviscid MR and (*d*) MR considering separation shock.

2. Theoretical methods and analyses

2.1. *Inviscid criteria*

The von Neumann and detachment criteria are illustrated by shock polar lines, as shown in figure 4(*a*). If the reflected shock polar line and incident shock polar line intersect at point A, then the flow deflection angle is the von Neumann criterion α_{vn}, which can be obtained from the pressure balance equation:

$$f_p(M_\infty, \pi/2) = f_p(M_\infty, \beta_{vn}) f_p(M_{vn}, \beta_{vnr}), \tag{2.1}$$

where β_{vn} is the incident shock angle, M_{vn} is the Mach number behind the incident shock and β_{vnr} is the local reflected shock angle, as shown in figure 4(*b*). The variables fulfil the following equations:

$$\left.\begin{aligned} f_\alpha(M_\infty, \beta_{vn}) &= f_\alpha(M_{vn}, \beta_{vnr}), \\ {M_{vn}}^2 \sin^2(\beta_{vn} - \alpha_{vn}) &= f_M(M_\infty, \beta_{vn}), \\ \tan\alpha_{vn} &= f_\alpha(M_\infty, \beta_{vn}), \end{aligned}\right\} \tag{2.2}$$

where f_p, f_α and f_M are functions expressed as follows:

$$\left.\begin{aligned} f_p(M, \beta) &= \frac{2\gamma}{\gamma+1} M^2 \sin^2\beta - \frac{\gamma-1}{\gamma+1}, \\ f_\alpha(M, \beta) &= \frac{2M^2 \sin^2\beta - 2}{[2 + M^2(\gamma + 1 - 2\sin^2\beta)]\tan\beta}, \\ f_M(M, \beta) &= \frac{2 + (\gamma-1)M^2 \sin^2\beta}{2\gamma M^2 \sin^2\beta - \gamma + 1}, \end{aligned}\right\} \tag{2.3}$$

The solution of α_{vn} does not exist in the Mach number range of $M_\infty < M_c$, where M_c is a critical Mach number, with $M_c \approx 2.2$. If the reflected shock polar line is tangent to the

y-axis at point B, as shown in figure 4(a), then the flow deflection angle is the detachment criterion α_D, which can be obtained from the following equations:

$$\left.\begin{aligned} {M_D}^2 \sin^2(\beta_D - \alpha_D) &= f_M(M_\infty, \beta_D), \\ f_\alpha(M_\infty, \beta_D) &= f_\alpha(M_D, \beta_{DM}), \end{aligned}\right\} \tag{2.4}$$

where β_D is the incident shock angle and M_D is the Mach number behind the incident shock, as shown in figure 4(c). In addition, β_{DM} is a critical shock angle for the attached shock, which can be obtained from the following equation (see Li & Ben-Dor 1996a):

$$\sin^2\beta_{DM} = \frac{1}{\gamma {M_D}^2}\left\{\frac{\gamma+1}{4}{M_D}^2 - 1 + \left[(\gamma+1)\left(1 + \frac{\gamma-1}{2}{M_D}^2 + \frac{\gamma+1}{16}{M_D}^4\right)\right]^{0.5}\right\}. \tag{2.5}$$

2.2. *Criteria considering viscosity*

The current study focuses on the shock reflections near the leading edge shown in figure 1. Because separation at a sharp leading edge differs fundamentally from separation of a boundary layer from a flat surface, on the one hand, FIT is employed to approximate the separation shock strength when the flow separates from the boundary layer, as shown in figure 1(b); on the other hand, the MEP principle is employed to approximate the separation shock strength when the flow separates from the leading edge, as shown in figure 1(c). Following the previous description of FIT, the separation shock strength can be computed by (1.1), the subsequent section mainly discusses the application of the MEP principle.

Because the MEP principle is proposed based on the assumption of asymmetric shock–shock interaction, the theoretical model needs to be established for a flow field with a separation bubble moving to a very upstream position and the leading-edge shock being totally replaced by separation shock. Assuming that the influences of the boundary layer and leading-edge shock are sufficiently weak compared with the separation bubble, the shock reflection mainly interacts with incident shock i, a known shock generated by a wedge, and separation shock i_s an unknown shock on the bottom plate. If incident shock i remains stable, as shown in figure 5(a), and the separation shock angle increases from β_s to β_s', then the RR solution on the shock polar line should move from α_r to α_r', accompanied by changes in reflected shocks r_s to r_s' and r to r', whereas in figure 5(b), because the reflected shock polar lines of the incident shock and separation shock have no intersection, the increase in β_s to β_s' only affects the MR solution of α_{r2} by changing r_s to r_s'.

Because, in the MR configuration, the polar lines show that α_{r2} does not affect α_{r1}, the whole flow field can be treated as three flow fields: Flow I, which is an inviscid flow determined by the Mach number and incident shock; Flow II, which is a very strong curved shock; and Flow III, which is a separation flow determined by the Mach number and separation shock, as shown in figure 6(a). A non-dimensional factor $\ddot{S}$ (see Wang *et al.* 2018; Xue *et al.* 2020) is employed to measure the total entropy production, as follows

$$\ddot{S} = \frac{\dot{S}}{C_v(\gamma-1)\rho_\infty M_\infty l\sqrt{\gamma R T_\infty}}, \tag{2.6}$$

where the variables in the denominator correspond to the incoming flow conditions, C_v is the specific heat capacity at constant volume and $\dot{S}$ is the total entropy production

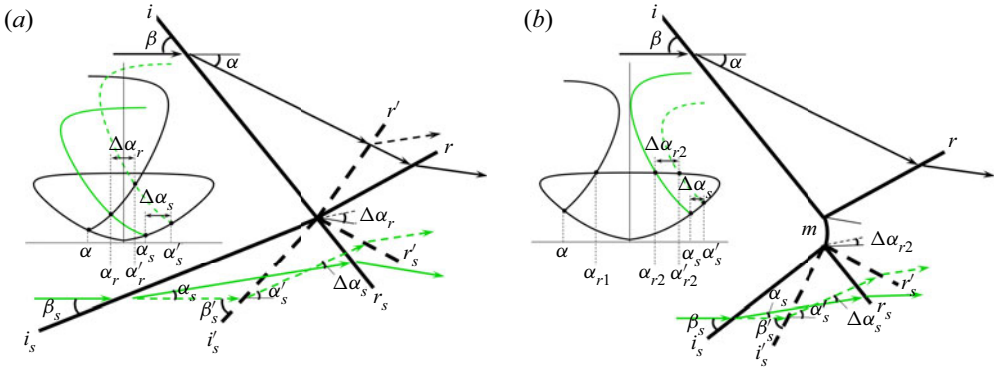

Figure 5. Influences of the separation shock strength on the reflected shock strength: (*a*) RR and (*b*) MR.

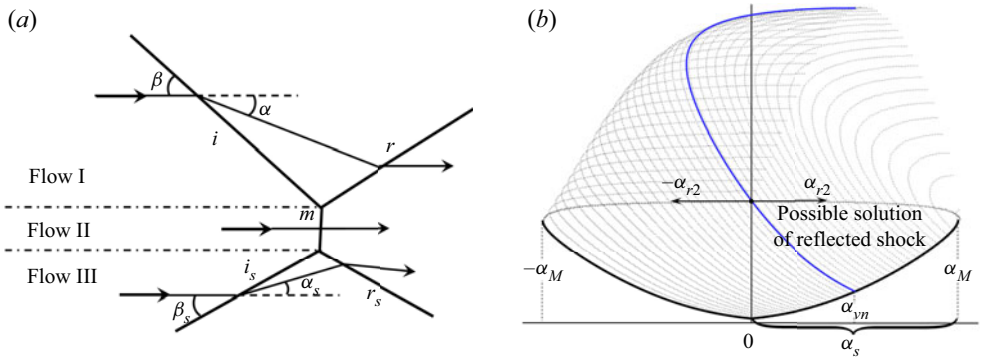

Figure 6. Simplified flow configurations and polar lines of possible solutions of separation shock: (*a*) flow configurations and (*b*) polar lines.

(see Li & Ben-Dor 1996*a*), such that

$$\dot{S} = \int_l \rho u \Delta s \, \mathrm{d}y, \tag{2.7}$$

where Δs is the local entropy production of flow crossing a shock wave, and is given by

$$\Delta s = -C_v(\gamma - 1)\ln(p_{02}/p_{01}). \tag{2.8}$$

In (2.8) p_{01} and p_{02} are the total pressures ahead and behind the shock wave, respectively. Assuming that the separation shock is a straight shock at the leading edge, the entropy factor $\ddot{S}_{MR}$ can be derived as follows:

$$\ddot{S}_{MR} = -f_{\dot{S}}(M_\infty, \beta_s)\left[1 + \frac{f_{\ddot{S}}(M_s, \beta_{sr})}{\ln f_{p0}(M_\infty, \beta_s)}\right], \tag{2.9}$$

where β_s is the separation shock angle, M_s is the Mach number behind the separation shock and β_{sr} is the local reflected shock angle of the separation shock, as shown in figure 4(*d*).

The function $f_{\ddot{S}}$ is derived as follows:

$$f_{\ddot{S}}(M,\beta)=\frac{f_\rho(M,\beta)\ln f_{p0}(M,\beta)\sqrt{f_M(M,\beta)f_T(M,\beta)}}{M\sin\beta\cos[\beta-\tan^{-1}f_\alpha(M,\beta)]},\tag{2.10}$$

where f_M, f_α and f_p have been given by (2.3), and f_ρ, f_T and f_{p0} are expressed as follows:

$$\left.\begin{aligned} f_\rho(M,\beta)&=\frac{(\gamma+1)M^2\sin^2\beta}{(\gamma-1)M^2\sin^2\beta+2},\\ f_T(M,\beta)&=\frac{f_p(M,\beta)}{f_\rho(M,\beta)},\\ f_{p0}(M,\beta)&=[f_p(M,\beta)]^{-(1/(\gamma-1))}[f_\rho(M,\beta)]^{\gamma/(\gamma-1)}. \end{aligned}\right\}\tag{2.11}$$

In addition, M_s and β_{sr} fulfil the pressure balance equation, and we write

$$f_p(M_\infty,\beta_{srs})=f_p(M_\infty,\beta_s)f_p(M_s,\beta_{sr}),\tag{2.12}$$

where β_{srs} is the strong shock angle of the Mach stem close to the interaction point, which fulfils the following equations:

$$\left.\begin{aligned} {M_s}^2\sin^2[\beta_s-\tan^{-1}f_\alpha(M_\infty,\beta_s)]&=f_M(M_\infty,\beta_s),\\ \tan^{-1}f_\alpha(M_\infty,\beta_s)+\tan^{-1}f_\alpha(M_\infty,\beta_{srs})&=\tan^{-1}f_\alpha(M_s,\beta_{sr}). \end{aligned}\right\}\tag{2.13}$$

If the possible flow deflection angle α_s of separation flow resides in the range of 0 to α_M, as shown in figure 6(*b*), the possible solution of reflected shock α_{r2} ranges from $-\alpha_M$ to α_M. Because the Mach stem is a very strong shock, it can be treated as a normal shock for computing the entropy, which is only related to the incoming Mach number. Notably, the incident shock is a known shock, and the separation shock angle β_s depends on M_∞ and α_s. Thus, the relation between $\ddot{S}_{MR}$ and α_s is established, based on which, the flow deflection angle α_s can be determined by $\ddot{S}_{MR}=$ *minimum* according to the MEP principle:

$$\left.\begin{aligned} \frac{\partial\ddot{S}_{MR}}{\partial\alpha_s}&=0,\\ \frac{\partial^2\ddot{S}_{MR}}{\partial\alpha_s^2}&\geq 0. \end{aligned}\right\}\tag{2.14}$$

The entropy factor line is helpful for understanding the prediction of the deflection angle in separation flow by the MEP principle. Three examples of $M_\infty=2$, 2.5 and 3 are shown in figure 7, in which relations between flow deflection angle α_s and entropy factor $\ddot{S}_{MR}$ are illustrated. The three minimum values of $\ddot{S}_{MR}$ which fulfil (2.14) for $M_\infty=2$, 2.5 and 3 exist at $\alpha_s=14.4^\circ$, 16.4° and 17.1°, respectively, corresponding to $\beta_s=44.6^\circ$, 38.5° and 34.5°. Comparing the three angles to the separation shock angles close to the interaction point of MR measured on the pictures in several recent studies: in the study of Tao *et al.* (2014), the measured angle is $\beta_s\approx 34^\circ$ for $M_\infty=3$ and in the study of Matheis & Hickel (2015), the measured angles are $\beta_s\approx 41^\circ$ for $M_\infty=2$ and $\beta_s\approx 34^\circ$ for $M_\infty=3$; in the study of Grossman & Bruce (2018), the measured angle is $\beta_s\approx 42^\circ$ for $M_\infty=2$; and in the study of Xue *et al.* (2020), the measured angles are $\beta_s\approx 43^\circ$ for $M_\infty=2$ and $\beta_s\approx 37^\circ$ for $M_\infty=2.5$. The comparisons are summarised in table 1. It is observed that the theoretical results of the MEP principle are close to the results in the

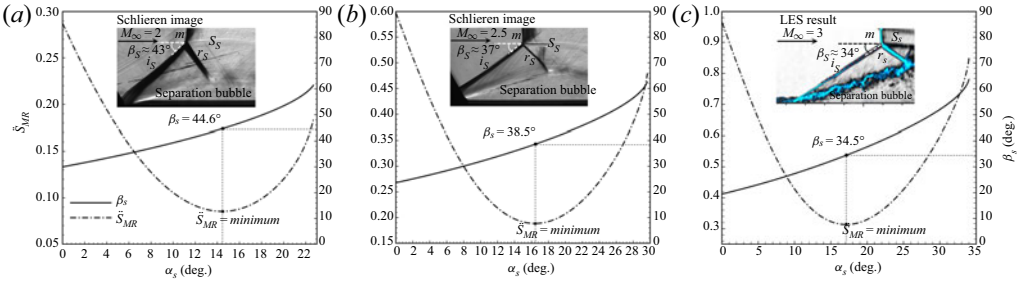

Figure 7. Comparison between current theoretical results and those in the literature: (*a*) $M_\infty = 2$ (see Xue *et al.* 2020), (*b*) $M_\infty = 2.5$ (see Xue *et al.* 2020) and (*c*) $M_\infty = 3$ (see Matheis & Hickel 2015).

M_∞	2	2.5	3
β_s based on MEP	44.6°	38.5°	34.5°
Tao *et al.* (2014)	\	\	≈34°
Matheis & Hickel (2015)	≈41°	\	≈34°
Grossman & Bruce (2018)	≈42°	\	\
Xue *et al.* (2020)	≈43°	≈37°	\

Table 1. Comparison between current theoretical results of separation shock angle in MR and those measured in the literature.

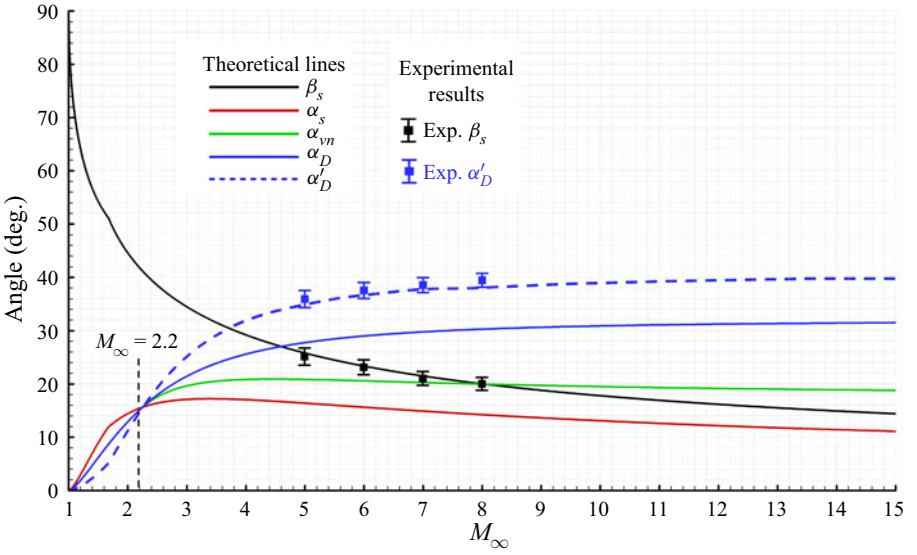

Figure 8. Comparison between theoretical lines and experimental results.

literature. However, the angles in the literature are smaller than the current results because all the shock reflections in the literature were strongly affected by the boundary layer, which did not fulfil the assumption of the MEP principle.

Because the incident shock–separation shock interaction shown in figure 1(*c*) could be assumed to be an asymmetric shock–shock interaction, a detachment criterion for the

RR-to-MR transition of the asymmetric shock–shock interaction can be determined (see Li, Chpoun & Ben-Dor 1999). The theoretical lines, including the von Neumann criterion α_{vn}, detachment criterion α_D and the MEP criterion α'_D lines, are summarised in figure 8. A critical Mach number $M_\infty \approx 2.2$ can be easily observed. On the one hand, when $M_\infty < 2.2$, the von Neumann criterion α_{vn} is not available, while the detachment criterion α_D is larger than MEP criterion α'_D, which means that MR might exist in $\alpha'_D < \alpha < \alpha_D$. On the other hand, when $M_\infty > 2.2$, α_D is smaller than α'_D, meaning that RR could exist in $\alpha_D < \alpha < \alpha'_D$ and the RR-to-MR transition possibly occurs at $\alpha > \alpha_D$. For high Mach numbers, the distinction between α_D and α'_D increasingly grows, and the flow deflection angle might be very large when the transition occurs, while much less information is available in the literature for the RR-to-MR transition on a plate in hypersonic flows. Therefore, the current experiments are performed in $M_\infty = 5$, 6, 7 and 8 flows, of which the experimental results agree well with the theoretical results, and the flow deflection angle of the RR-to-MR transition is very close to the MEP criterion α'_D, as shown in figure 8. The current experiments are discussed in the following section.

3. Experiments and analyses

3.1. *Experimental set-up*

Experiments were performed in the NHW hypersonic wind tunnel of Nanjing University of Aeronautics and Astronautics. The wind tunnel runs in a 'blow-down-to-vacuum' mode, which can be used to perform tests at 0.04–1.0 MPa total pressure, 288–685 K plenum temperature and 6.47×10^5–2.24×10^7 m^{-1} unit Reynolds number with 7–10 s of running time (see Wang, Xue & Tian 2017). The converging–diverging nozzle (exit diameter of 500 mm) mounted in the test section is interchangeable and provides nominal free-stream Mach numbers from 4 to 8. Two glass windows (diameter of 300 mm) are embedded in two sides of the test section walls for optical access. In addition, nozzles for Mach numbers 5, 6, 7 and 8 are employed in the current experiments.

The test model is a rotatable wedge (40° apex angle and 140 mm width) over a surface plate (160 mm width and 700 mm length) with a sharp leading edge (15° apex angle) for generating incident shock and separation shock, in which the flow deflection angle can be continuously changed from 0° to 40° through a high-precision stepping motor, as shown in figure 9. Nine Kulite XTEL-190M fast-response transducers are mounted along the central line of the surface plate and wedge bottom, which acquire data at a rate of 50 kHz with a 10 s sampling time using data acquisition cards. An NAC (NAC Image Technology) Hotshot high-speed camera operating at a frame rate of 5 kHz with a 6 s sampling time and a resolution of 600 × 438 pixels is employed to take schlieren images.

Because Mach waves will be propagating inward and reducing the region of the interaction that can be considered two-dimensional flow, as shown in figure 9(*b*), $\bar{W}$ is defined to represent the percentage of two-dimensional flow. In addition, two non-dimensional variables $\bar{H}$ and $\bar{X}$ are defined to describe the vertical and horizontal distances between the wedge and the plate, respectively:

$$\left.\begin{aligned} \bar{W} &= \Delta w / W_{plate}, \\ \bar{H} &= \Delta h / W_{wedge}, \\ \bar{X} &= \Delta x / W_{wedge}, \end{aligned}\right\} \tag{3.1}$$

where Δw, Δh, Δx, W_{plate} and W_{wedge} are marked in figure 9(*b*). The shock impingement location on the plate is not in the same position owing to the continuously increasing

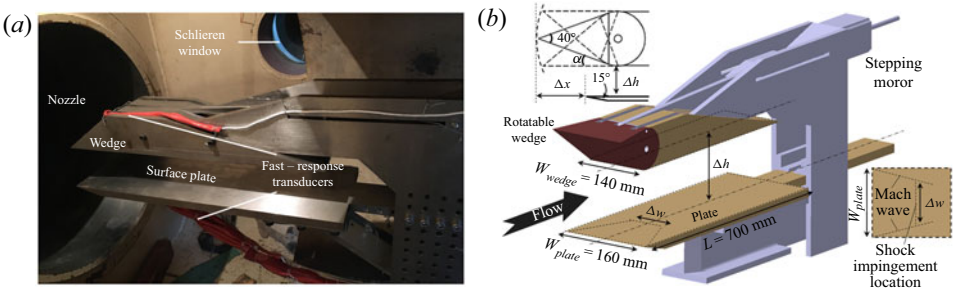

Figure 9. Test model: (*a*) real model in a wind tunnel and (*b*) illustration of the rotatable wedge.

Tests	M_∞	$Re \times 10^{-6}$ m	$\bar{H}$	$\bar{X}$	$\bar{W}$
Case 1	5	7.02	0.464	0.286	0.705–0.883
Case 2	5	2.23	0.464	0.429	0.755–0.934
Case 3	5	2.32	0.464	0.286	0.705–0.883
Case 4	5	2.32	0.464	0.143	0.652–0.832
Case 5	5	2.45	0.464	0.000	0.601–0.791
Case 6	5	2.46	0.464	−0.143	0.551–0.739
Case 7	5	2.43	0.179	0.286	0.857–0.936
Case 8	5	2.56	0.321	0.286	0.785–0.908
Case 9	5	2.49	0.607	0.286	0.627–0.865
Case 10	5	1.77	0.464	0.286	0.705–0.883
Case 11	5	3.97	0.464	0.286	0.705–0.883
Case 12	5	5.41	0.464	0.286	0.705–0.883
Case 13	5	6.55	0.464	0.286	0.705–0.883
Case 14	6	4.95	0.464	0.286	0.737–0.901
Case 15	7	2.29	0.464	0.286	0.764–0.911
Case 16	8	1.38	0.464	0.286	0.791–0.920

Table 2. Flow conditions of the experiments.

incident shock angle during one test, thus $\bar{W}$ changes from a lower value to a higher one with the interaction region moving upstream.

The current experiments were performed in a low-enthalpy wind tunnel (the total temperature was set at 600 ± 15 K for each test), thus the real gas effects could be neglected. The free-stream turbulence intensities of the wind tunnel for Mach number 5, 6, 7 and 8 are 0.022, 0.023, 0.025 and 0.025, respectively. More flow conditions are summarised in table 2. An algorithm program for schlieren image quantisation based on the grey level (see Xue, Wang & Cheng 2018) is employed to compute the separation shock angles, and experimental uncertainties are characterised by the standard deviation. The experimental uncertainties are contributed by various factors, e.g. the free-stream turbulence, white noise and the possible error of image quantisation (affected by image quality).

3.2. *Evolution of the RR-to-MR transition near the leading edge*

The evolution of the flow field with increasing incident shock angle is shown in figure 10, where the free-stream Mach number is $M_\infty = 5$, and the unit Reynolds number is

$Re = 7.02 \times 10^6$ m^{-1}, $\bar{H} = 0.464$ and $\bar{X} = 0.286$. Eight pressure transducers named T1 to T8 are mounted on the plate in the interaction region, and one named T0 is mounted on the wedge bottom behind the incident shock. The transducer positions are marked in the schlieren images, as shown in figure 10. The shock reflection is undoubtedly affected by the leading-edge shock and boundary layer when $\alpha = 25^\circ$, which corresponds to the flow pattern shown in figure 1(*b*). The separation shock angle $\beta_{s.Exp} \approx 16.1^\circ \pm 0.6^\circ$ obtained from schlieren images is between $\beta_{s.FIT0} \approx 15.2^\circ$ and $\beta_{s.FIT1} \approx 17.6^\circ$ computed by (1.1) with $F(\bar{x})_{lam0} \approx 0.81$ and $F(\bar{x})_{lam1} \approx 1.47$, respectively, indicating that FIT is applicable well when the flow on the plate separates from the boundary layer. In the laminar separation region ahead of the shock impingement location, the static pressure on the plate, T1 to T4 shown in figure 10(*a*), stay in low values and fluctuate with small amplitudes (small standard deviations), while the amplitudes grow distinctly at T5 to T8 with a sharp pressure increase trend, demonstrating that the shock impingement location reduces flow stability and damages the laminar boundary layer. The separation bubble moves continuously upstream with increasing α, and the separation shock seems to interact with the leading-edge shock l_e when $\alpha = 30^\circ$, as shown in figure 10(*c*). The shock impingement location also moves upstream, causing T1 to T4 increase in turn with relatively large amplitudes, and T5 to T8 decrease in turn with relatively small amplitudes. Finally, l_e is totally replaced by i_s for $\alpha > 33^\circ$ because i_s is a stronger shock wave than l_e. Then, the separation bubble moves to the most upstream position and replaces the boundary layer, which corresponds to the flow pattern shown in figure 1(*c*). Meanwhile, the shock impingement location moves to the T1 and T2 positions, and leads to very large amplitudes of T1 and T2 pressures and relatively small amplitudes of T3 to T8, indicating that a reattached flow follows the interaction region. The RR-to-MR transition occurs at $\alpha \approx 36.1^\circ$ with the appearance of a very short Mach stem m.

The comparisons between the theoretical results and experiments are summarised in figure 11. As shown in figure 11(*a*), the minimum value of $\ddot{S}_{MR}$ exists at $\alpha_{s.MEP} \approx 16.4^\circ$, corresponding to $\beta_{s.MEP} \approx 25.8^\circ$, which agrees well with the separation shock angle $\beta_{s.Exp} \approx 25.2^\circ \pm 0.9^\circ$ obtained from the schlieren images. Figure 11(*b*) demonstrates that the separation shock angle in MR is distinctly larger than that in RR, and that the theoretical model of FIT is applicable to flow pattern before the separation bubble moves to the leading edge while the MEP principle is applicable to the flow pattern after the separation bubble moves to the leading edge.

Figures 12 and 13 show the comparison between RR-to-MR and MR-to-RR transitions. Based on the schlieren images, both transitions occur at $\alpha \approx 36.1^\circ$, and shock reflections are almost characterised by the same configurations when the test model generates the same flow deflection angle. Figure 13 gives the time histories of pressures by Kulite transducers and corresponding data analysis with α increasing and decreasing. During the test, the wedge angle changes almost linearly, from 24° to 40° or from 40° to 24° within 2 s. As shown in figure 13(*a*), the incident shock strength, represented by T0, increases almost linearly, driving the separation region to move upstream and downstream, resulting in gradual changes for T1 to T8. When the transducers experience upstream movement of the separation bubble, the pressures increase in turn and then decrease in turn, with the peaks growing higher. When the transducers experience downstream movement of the separation bubble, the reversible process is nearly symmetric. Therefore, the shock reflection of the RR-to-MR or MR-to-RR transition near the leading edge does not present a distinct hysteresis.

Because transducer T1 experiences the separation bubble and the shock impingement location during 1.8 s to 3.6 s, the amplitude is distinctly larger than those of T2 to T8,

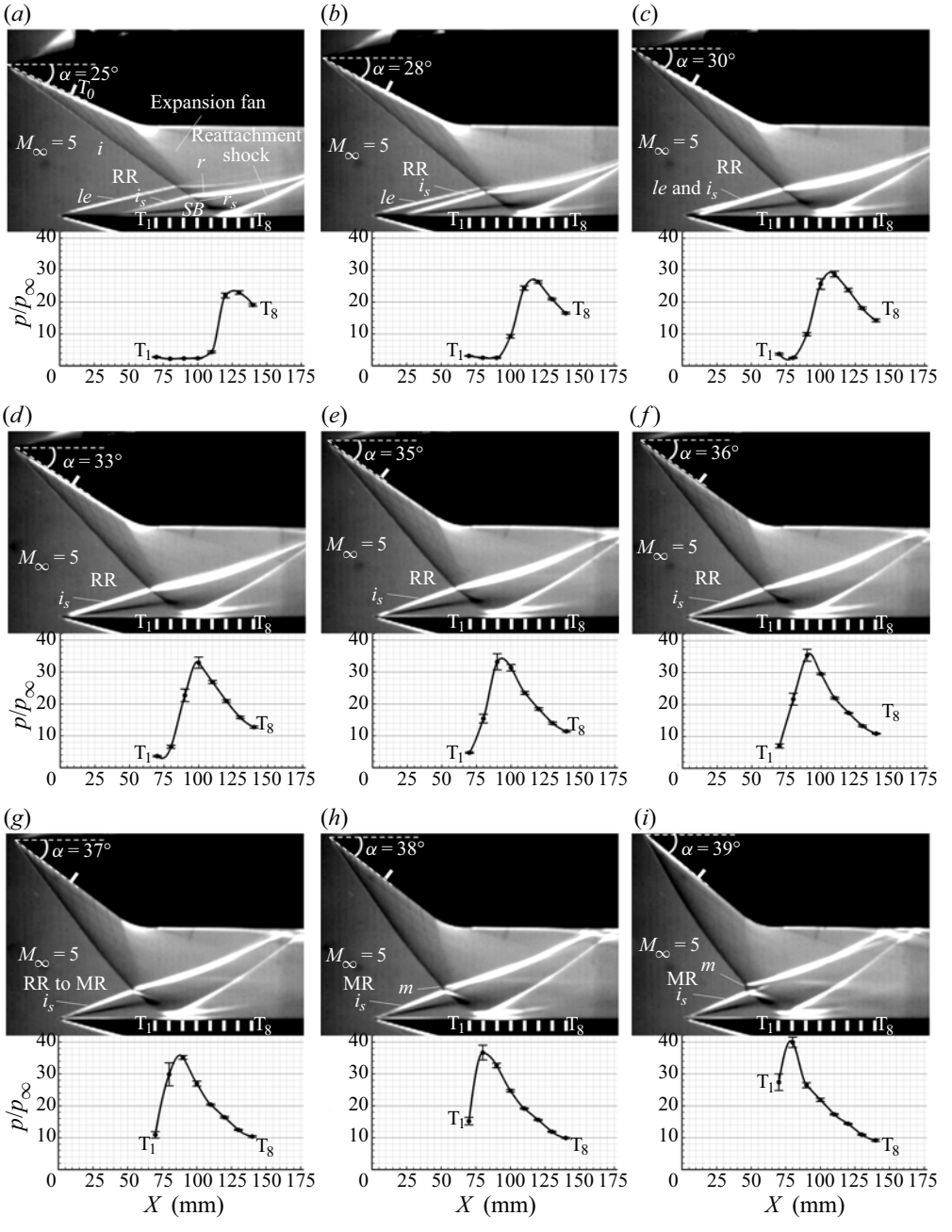

Figure 10. Evolution of the flow field with increasing incident shock angle ($M_\infty = 5$, $Re = 7.02 \times 10^6$ m^{-1}, $\bar{H} = 0.464$ and $\bar{X} = 0.286$): (*a*) $\alpha = 24^\circ$, (*b*) $\alpha = 28^\circ$, (*c*) $\alpha = 30^\circ$, (*d*) $\alpha = 33^\circ$, (*e*) $\alpha = 35^\circ$, (*f*) $\alpha = 36^\circ$, (*g*) $\alpha = 37^\circ$, (*h*) $\alpha = 38^\circ$ and (*i*) $\alpha = 39^\circ$.

which have been residing in the downstream reattached flow. Notably, although the amplitude of T1 is very large with noise (the pressure sampling frequency is 5×10^4 Hz), no distinct dominant frequency occurs below 10^4 Hz according to the fast Fourier transform. From the power spectral density (PSD) map, as shown in figure 13(*b*),

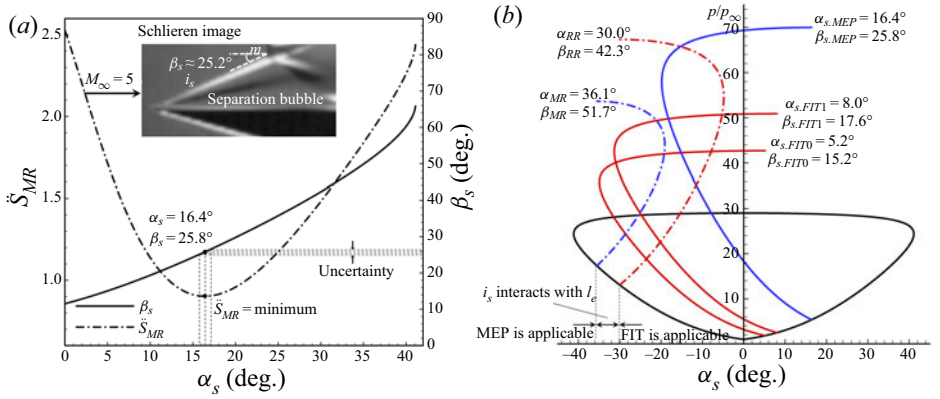

Figure 11. Comparison between theoretical results and experiments ($M_\infty = 5$, $Re = 7.02 \times 10^6$ m^{-1}, $\bar{H} = 0.464$ and $\bar{X} = 0.286$): (*a*) entropy factor line and (*b*) shock polar lines.

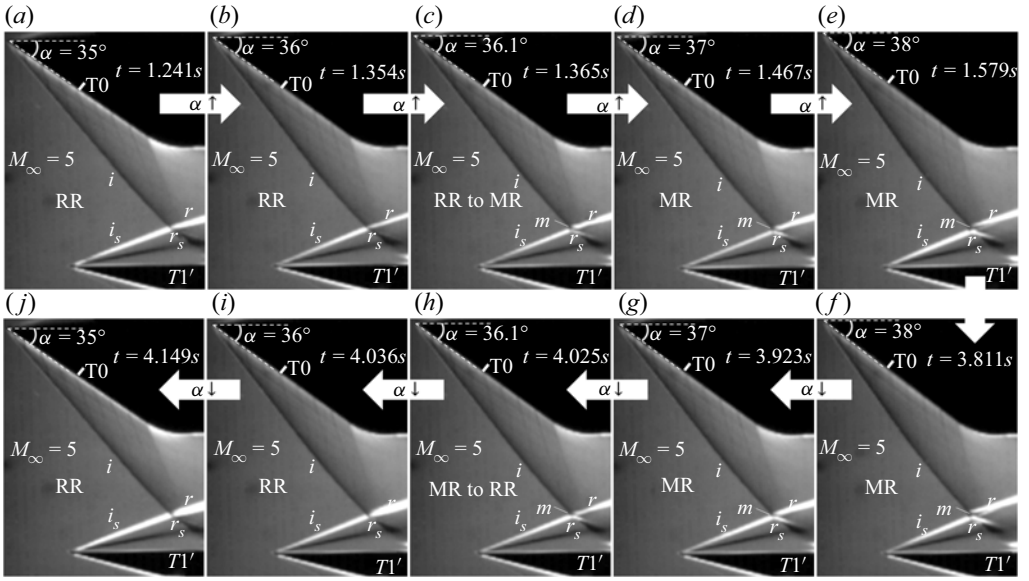

Figure 12. Evolution of the flow field with α increasing and decreasing ($M_\infty = 5$, $Re = 7.02 \times 10^6$ m^{-1}, $\bar{H} = 0.464$ and $\bar{X} = 0.286$): (*a*) $\alpha = 35°$, (*b*) $\alpha = 36°$, (*c*) $\alpha = 36.1°$, (*d*) $\alpha = 37°$, (*e*) $\alpha = 38°$, (*f*) $\alpha = 38°$, (*g*) $\alpha = 37°$, (*h*) $\alpha = 36.1°$, (*i*) $\alpha = 36°$ and (*j*) $\alpha = 35°$.

the pressure of T1 in laminar separation region shows no obvious frequency component when $t < 1.8$ s and $t > 3.6$ s, and T1 mainly fluctuates during 1.8 s to 3.6 s with most of the frequency components evenly spread in the range of 1 to 10^4 Hz, indicating that the laminar flow might be damaged by the shock impingement during 1.8 s to 3.6 s. In addition, there is no large scale shock oscillation observed in the flow configuration, thus the separation bubble and separation shock are relatively steady.

The pressure fluctuations of the transducers are related to free-stream turbulence and white noise, while the large amplitudes are mostly affected by the movement of the shock impingement location, which can be observed from the standard deviation of time–position map shown in figure 13(*c*). Obviously, the movement of the shock impingement location

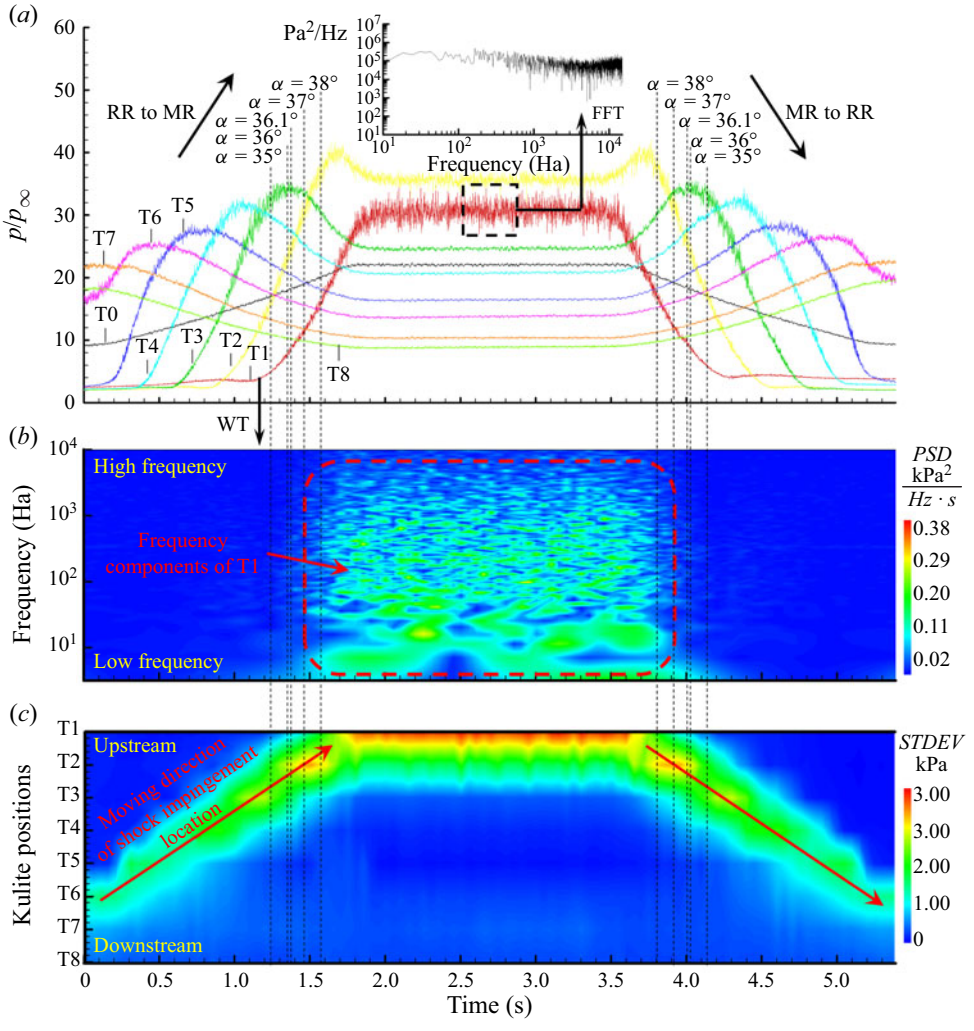

Figure 13. Static pressure on plate and corresponding data analysis with α increasing and decreasing ($M_\infty = 5$, $Re = 7.02 \times 10^6$ m^{-1}, $\bar{H} = 0.464$ and $\bar{X} = 0.286$): (*a*) time histories of Kulite transducers (T0 to T8), (*b*) time–frequency map of wavelet transform (WT) for illustrating PSD and (*c*) time–position map for illustrating standard deviation (STDEV).

causes a large pressure amplitude, which grows distinctly larger (T2 position) with the RR-to-MR transition ($\alpha \approx 36^\circ$) when the shock impingement location moves upstream, and the reversible process shows the opposite trend. Therefore, the flow instability depends on the location of the incident shock impingement, and it may be increased by the RR-to-MR transition. Because the RR-to-MR transition agreed well with MEP principle, the criterion based on this principle might be useful for predicting the instability of incident shock–separation shock interaction near the leading edge.

3.3. *The influences of wedge positions*

To investigate the influences of wedge positions on shock reflections, the following tests were conducted at $M_\infty = 5$ and $Re = 2.2$–2.6×10^6 m^{-1} with $\bar{X}$ decreasing from 0.429

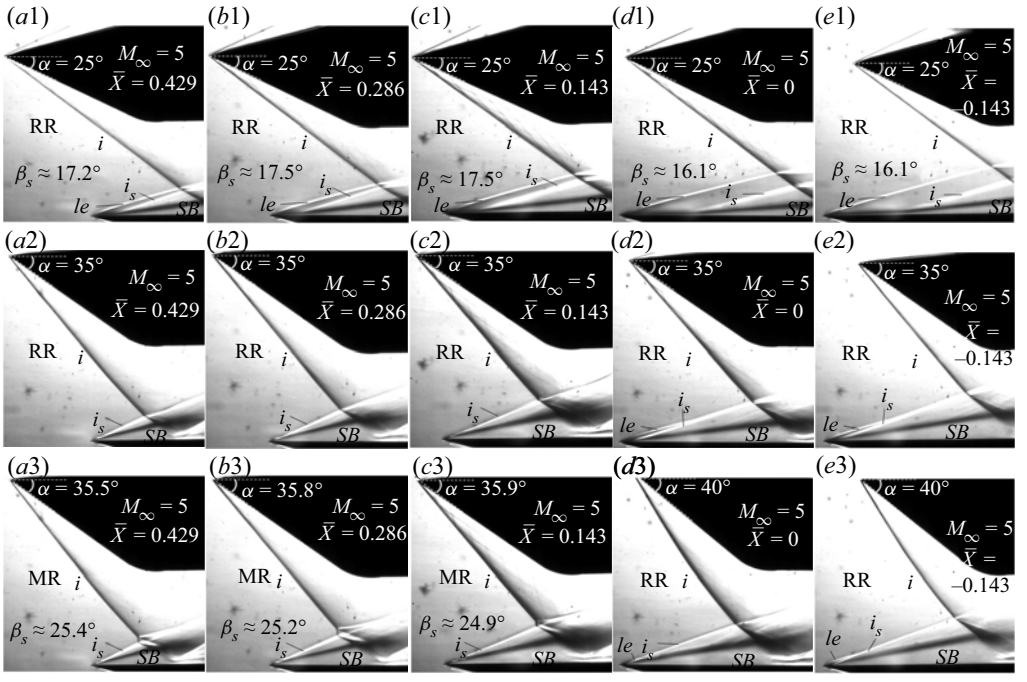

Figure 14. Influence of $\bar{X}$ on shock reflections ($M_\infty = 5$, $Re = 2.2$–2.6×10^6 m^{-1} and $\bar{H} = 0.464$): ($a1$–$a3$) $\bar{X} = 0.429$, ($b1$–$b3$) $\bar{X} = 0.286$, ($c1$–$c3$) $\bar{X} = 0.143$, ($d1$–$d3$) $\bar{X} = 0$ and ($e1$–$e3$) $\bar{X} = -0.143$.

to -0.143, as shown in figure 14, and $\bar{H}$ increasing from 0.179 to 0.607, as shown in figure 15. It can be observed from figures 14($a1$), 14($b1$), 14($c1$), 14($d1$) and 14($e1$) that the separation shock angles change in a small range before l_e coincides with i_s, indicating that the separation shock strength exerts weak effects by decreasing $\bar{X}$. In the cases of $\bar{X} = 0.429$, $\bar{X} = 0.286$ and $\bar{X} = 0.143$, RR-to-MR transitions occur at $\alpha \approx 35.7^\circ \pm 0.4^\circ$, whereas transitions do not occur in the cases of $\bar{X} = 0$ and $\bar{X} = -0.143$. Figures 14($d2$) and 14($e2$) show that the separation bubble does not reach the most upstream position and that l_e is not replaced by i_s when $\alpha = 35^\circ$, meaning that the flows on the plate still separate from the boundary layer rather than the leading edge. Thus, the separation shock is not strong enough to trigger an RR-to-MR transition. A similar phenomenon can be observed from figure 15($d2$) in which the RR-to-MR transition does not occur in the case of $\bar{H} = 0.607$ because the separation bubble does not reach the most upstream position. Figures 15($a2$) and 15($a3$) show that the occurrence of the RR-to-MR transition is replaced by an unstart flow field because the model generates too much compression when $\bar{H}$ decreases to 0.179.

Figures 14 and 15 demonstrate that the wedge positions strongly affect the shock reflections on the plate near the leading edge. The RR-to-MR transition does not occur with a relatively small $\bar{X}$ or high $\bar{H}$ because the separation bubble cannot reach the leading-edge position. This can be explained by the theoretical models. On one hand, FIT is applicable when flow on the plate separates from the boundary layer, and the separation shock strength of the FIT result is too weak to trigger an RR-to-MR transition, on the other hand, the separation shock strength of the MEP result is strong enough, while the MEP principle is applicable only if the flow on the plate separates from the leading edge. Therefore, the RR-to-MR transition is much harder to observe when flow separates from the boundary layer rather than from the leading edge.

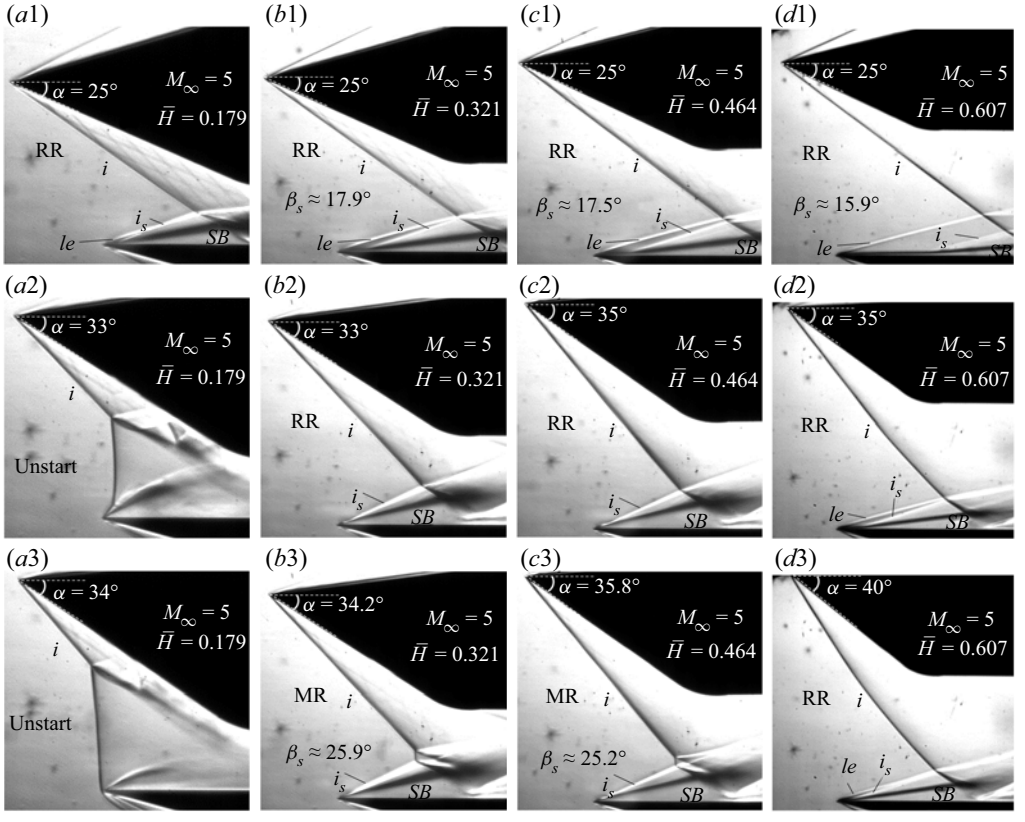

Figure 15. Influence of $\bar{H}$ on shock reflections ($M_\infty = 5$, $Re = 2.2$–2.6×10^6 m^{-1} and $\bar{X} = 0.286$): (*a*1–*a*3) $\bar{H} = 0.179$, (*b*1–*b*3) $\bar{H} = 0.321$, (*c*1–*c*3) $\bar{H} = 0.464$ and (*d*1–*d*3) $\bar{H} = 0.607$.

3.4. *The influences of Reynolds and Mach numbers*

To investigate the influences of Reynolds and Mach numbers on shock reflections, further tests were conducted at $\bar{H} = 0.464$ and $\bar{X} = 0.286$ with Re increasing from 1.77×10^6 m^{-1} to 6.55×10^6 m^{-1}, as shown in figure 16, and M_∞ increasing from 5 to 8, as shown in figure 17. It can be observed from figure 16 that when flow separates from the boundary layer, the separation shock angle is $\beta_{s.Exp} \approx 16.4° \pm 0.5°$, while it increases to $\beta_{s.Exp} \approx 24.9° \pm 0.6°$ with the RR-to-MR transitions occurring at $\alpha \approx 35.8° \pm 0.5°$. Thus, the separation shock angles in the configurations, before and after the separation bubble moves to the leading-edge position, are not as sensitive to the Reynolds number. Figure 17 shows that the separation shock angle decreases with increasing Mach number, and for each Mach number, the separation shock angle of flow separating from the leading edge is distinctly larger than that from the boundary layer. Therefore, the Mach number exerts a much stronger influence on shock reflection near the leading edge than the Reynolds number. The flow deflection angles $\alpha \approx 35.8° \pm 0.7°$, $37.8° \pm 0.7°$, $38.1° \pm 0.6°$ and $38.9° \pm 0.6°$ of the RR-to-MR transitions for $M_\infty = 5$, 6, 7 and 8 agree well with the MEP criterion angles of $\alpha \approx 34.9°$, $37.1°$, $37.5°$ and $38.2°$ based on the MEP results, respectively. The RR-to-MR transitions are delayed in turn with increasing Mach number, and the transition does not occur before the separation bubble moves to the leading-edge position. Figure 18 gives a comparison between the theoretical and experimental results, demonstrating that the separation shock angle in

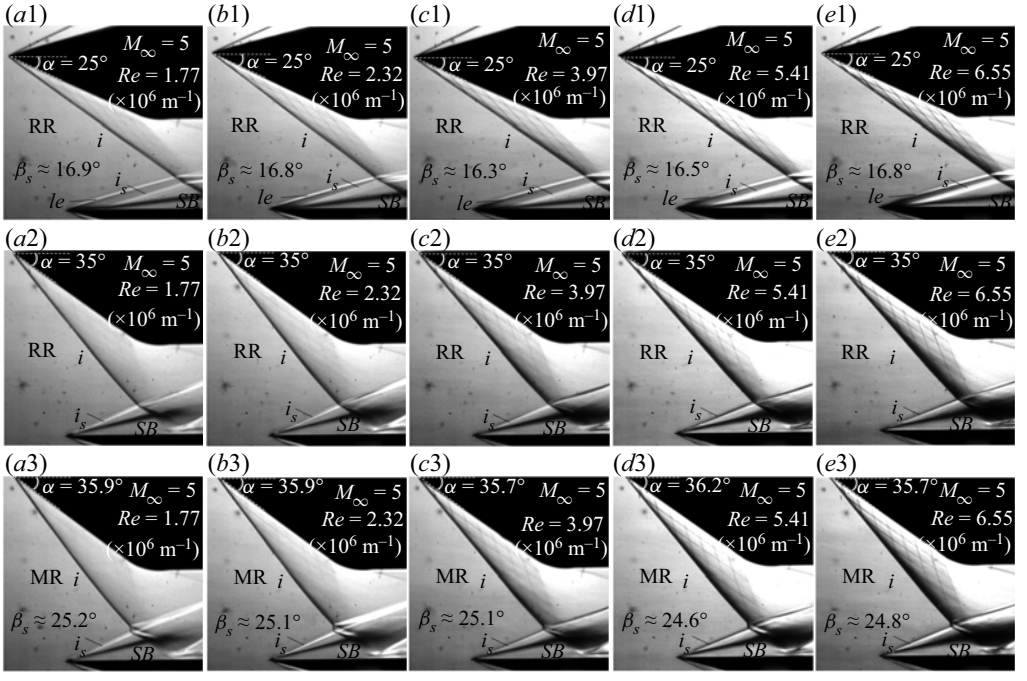

Figure 16. Influence of Re on shock reflections ($M_\infty = 5$, $\bar{H} = 0.464$ and $\bar{X} = 0.286$): ($a1$–$a3$) $Re = 1.77 \times 10^6$ m^{-1}, ($b1$–$b3$) $Re = 2.32 \times 10^6$ m^{-1}, ($c1$–$c3$) $Re = 3.97 \times 10^6$ m^{-1}, ($d1$–$d3$) $Re = 5.41 \times 10^6$ m^{-1} and ($e1$–$e3$) $Re = 6.55 \times 10^6$ m^{-1}.

the MR configuration for each Mach number agrees well with the MEP result. Because the MEP of shock reflection corresponds to the maximum total pressure recovery, the separation flow seems to choose a configuration that produces the smallest possible flow loss.

4. Conclusions

The current study theoretically and experimentally investigates the shock reflections on a plate near the leading edge in hypersonic flows. The theoretical method employs FIT and the MEP principle to analyse the separation shock strength of flow separated from the boundary layer and flow separated from the leading edge, respectively. The influences of wedge positions, Reynolds numbers and Mach numbers on shock reflections are investigated by careful tests. Accordingly, the following conclusions are obtained.

The shock reflection of hypersonic flow on a plate separated from the boundary layer is distinctly different from that separated from the leading edge. On one hand, when the separation bubble does not reach the most upstream position, the flow separated from the boundary layer could be treated as a free interaction, and the separation shock strength agrees well with the FIT result. On the other hand, when the separation bubble has reached the most upstream position, the flow separated from the leading edge could be treated as a shock–shock interaction, and the separation shock strength agrees well with the MEP result. The Reynolds number is not as sensitive to the shock reflections, and the separation shock strength mostly depends on the Mach number. The current experiments prove the theoretical results in the flows with Mach numbers 5, 6, 7 and 8, which are summarised in table 3. In addition, the inviscid criteria α_{vn} and α_D do not apply well to the prediction

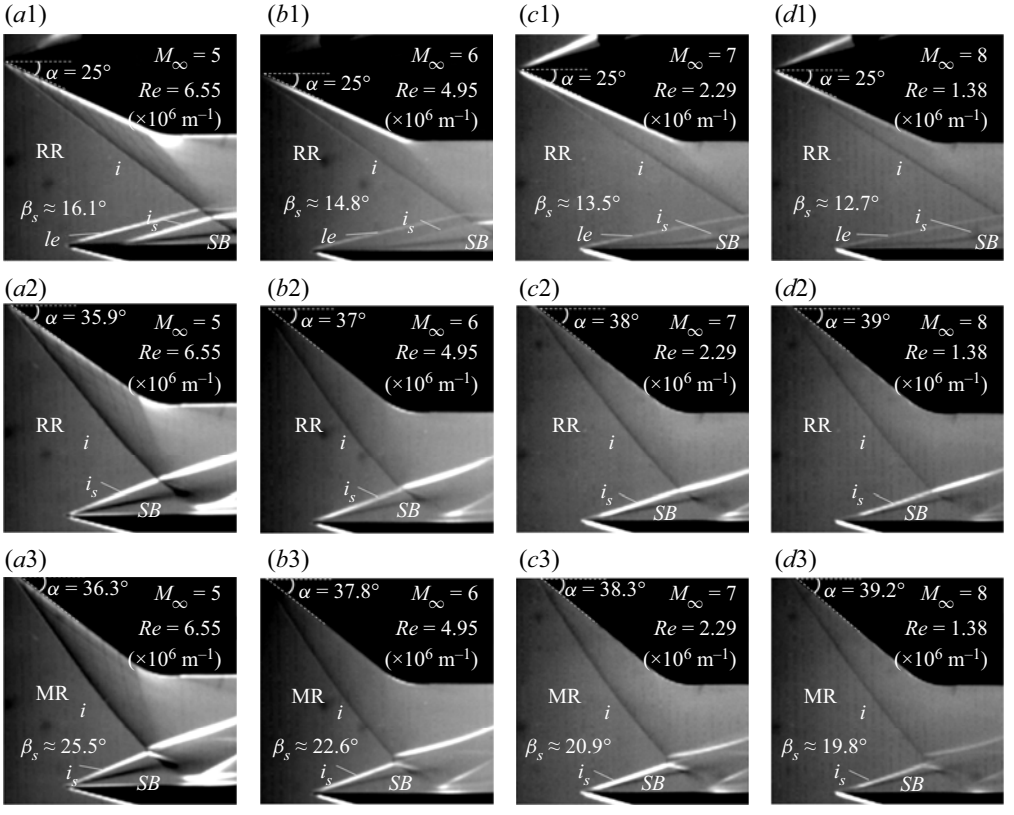

Figure 17. Influence of M_∞ on shock reflections ($\bar{H} = 0.464$ and $\bar{X} = 0.286$): (*a*1–*a*3) $M_\infty = 5$, $Re = 6.55 \times 10^6$ m^{-1}, (*b*1–*b*3) $M_\infty = 6$, $Re = 4.95 \times 10^6$ m^{-1}, (*c*1–*c*3) $M_\infty = 7$, $Re = 2.29 \times 10^6$ m^{-1} and (*d*1–*d*3) $M_\infty = 8$, $Re = 1.38 \times 10^6$ m^{-1}.

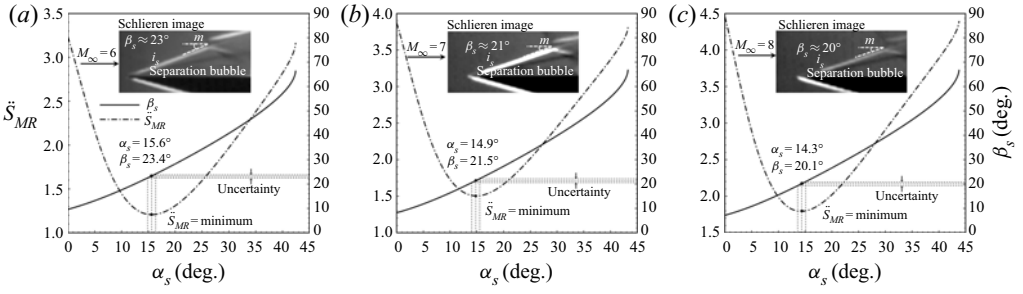

Figure 18. Comparison between theoretical lines and experimental results: (*a*) $M_\infty = 6$, (*b*) $M_\infty = 7$ and (*c*) $M_\infty = 8$.

of the RR-to-MR transition near the leading edge on the plate, therefore, the criterion α'_D based on the MEP principle is employed to predict the RR-to-MR transition. For each Mach number in table 3, compared with the inviscid von Neumann criterion α_{vn} and detachment criterion α_D, the criterion α'_D is much closer to experimental result of α_{Exp}.

The RR-to-MR transition occurs much more easily at flow separated from the leading edge than at the boundary layer because the MEP result is much larger than the FIT result, and in fact, the RR-to-MR transition with flow separating from the boundary layer is

M_∞	5	6	7	8
α_{vn}	20.9°	20.6°	20.3°	20.0°
α_D	27.8°	29.0°	29.8°	30.3°
α'_D	34.9°	37.1°	37.5°	38.2°
α_{Exp}	$35.8° \pm 0.7°$	$37.8° \pm 0.7°$	$38.1° \pm 0.6°$	$38.9° \pm 0.6°$

Table 3. Theoretical criteria and experimental results.

never observed in the current experiments. When the separation bubble moves to the most upstream position, the shock reflection of the RR-to-MR or MR-to-RR transition near the leading edge does not present a distinct hysteresis. The wedge position strongly affects the RR-to-MR transition because the separation bubble might not reach the most upstream position with relatively small $\bar{X}(\bar{X} < 0)$ and high $\bar{H}(\bar{H} > 0.607)$, resulting in flow on the plate separated from the boundary layer. In addition, for a relatively low $\bar{H}(\bar{H} < 0.179)$, the flow field is possibly unstarted when the flow deflection angle approaches the MEP criterion.

Therefore, FIT and the MEP principle respectively contribute to the flow separated from boundary layer and the leading edge, and the criterion based on MEP principle might be useful for predicting the instability of some flow interactions near the leading edge, e.g. hypersonic inlets.

Acknowledgements. This support is gratefully acknowledged. We thank Professor S. Zhiwei, H. Da and technician B. Jifa for assistance in all the experiments.

Funding. This work was supported by the National Natural Science Foundation of China (grant numbers 12072157, 12002163 and 51776096), Natural Science Foundation of Jiangsu Province (grant number BK20200408) and China Postdoctoral Science Foundation (grant numbers 2019TQ0147 and 2020M671472).

Declaration of interests. The authors report no conflict of interest.

Author ORCIDs.
Longsheng Xue https://orcid.org/0000-0001-5137-7367;
Chengpeng Wang https://orcid.org/0000-0003-3865-5080.

References

Babinsky, H. & Harvey, J.K. 2011 *Shock Wave-Boundary-Layer Interactions*. Cambridge University Press.

Chapman, D.R., Kuehn, D.M. & Larson, H.K. 1958 Investigation of separated flows in supersonic and subsonic streams with emphasis on the effect of transition. *Tech. Rep.* 1356. NACA.

Chpoun, A., Passerel, D., Li, H. & Ben-Dor, G. 1995 Reconsideration of oblique shock wave reflections in steady flows. Part 1. Experimental investigation. *J. Fluid Mech.* **301**, 19–35.

Erdos, J. & Pallone, A. 1962 Shock-boundary layer interaction and flow separation. In *Proceedings of the 1962 Heat Transfer and Fluid Mechanics Institute*, vol. 15, pp. 239–254. Stanford University Press.

Giepman, R.H.M., Schrijer, F.F.J. & van Oudheusden, B.W. 2018 A parametric study of laminar and transitional oblique shock wave reflections. *J. Fluid Mech.* **844**, 187–215.

Grossman, I.J. & Bruce, P.J.K. 2018 Confinement effects on regular-irregular transition in shock-wave-boundary-layer interactions. *J. Fluid Mech.* **853**, 171–204.

Hakkinen, R.J., Greber, I., Trilling, L. & Abarbanel, S.S. 1959 The interaction of an oblique shock wave with a laminar boundary layer. *Tech. Rep.* NASA Memo 2-18-59W.

Li, H. & Ben-Dor, G. 1996*a* Application of the principle of minimum entropy production to shock wave reflection. Part I. steady flow. *J. Appl. Phys.* **80**, 2027–2037.

Li, H. & Ben-Dor, G. 1996*b* Application of the principle of minimum entropy production to shock wave reflection. Part II. unsteady flow. *J. Appl. Phys.* **80**, 2038–2048.

LI, H., CHPOUN, A. & BEN-DOR, G. 1999 Analytical and experimental investigations of the reflection of asymmetric shock waves in steady flows. *J. Fluid Mech.* **390**, 25–43.

MATHEIS, J. & HICKEL, S. 2015 On the transition between regular and irregular shock patterns of shock-wave/boundary-layer interactions. *J. Fluid Mech.* **776**, 200–234.

VON NEUMANN, J. 1943 Oblique reflection of shocks. *Tech. Rep.* 12. Navy Department, Bureau of Ordnance, Washington DC.

VON NEUMANN, J. 1945 Refraction, intersection and reflection of shock waves. *Tech. Rep.* 203. Navy Department, Bureau of Ordnance, Washington DC.

SRIRAM, R., SRINATH, L., DEVARAJ, M.K.K. & JAGADEESH, G. 2016 On the length scales of hypersonic shock-induced large separation bubbles near leading edges. *J. Fluid Mech.* **806**, 304–355.

TAO, Y., FAN, X.Q. & ZHAO, Y.L. 2014 Viscous effects of shock reflection hysteresis in steady supersonic flows. *J. Fluid Mech.* **759**, 134–148.

WANG, C.P., XUE, L.S. & CHENG, K.M. 2018 Application of the minimum entropy production principle to shock reflection induced by separation. *J. Fluid Mech.* **857**, 784–805.

WANG, C.P., XUE, L.S. & TIAN, X.A. 2017 Experimental characteristics of oblique shock train upstream propagation. *Chin. J. Aeronaut.* **30**, 663–676.

XUE, L.S., SCHRIJER, F.F.J., VAN OUDHEUSDEN, B.W., WANG, C.P., SHI, Z.W. & CHENG, K.M. 2020 Theoretical study on regular reflection of shock wave-boundary layer interactions. *J. Fluid Mech.* **899**, A30.

XUE, L.S., WANG, C.P. & CHENG, K.M. 2018 Dynamic characteristics of separation shock in an unstarted hypersonic inlet flow. *AIAA J.* **56**, 2484–2490.

ZHELTOVODOV, A.A. 1996 Shock waves/turbulent boundary-layer interactions – fundamental studies and applications. *Tech. Rep.* 96. AIAA Paper.

ZHELTOVODOV, A.A. & YAKOVLEV, V.N. 1986 Stages of development, gas dynamic structure and turbulence characteristics of turbulent compressible separated flows in the vicinity of 2-D obstacles. *Tech. Rep.* 27. Inst. Theor. Appl. Mech. (ITAM).